Journal of Alloys and Compounds 1017 (2025) 178974

Contents lists available at ScienceDirect

Journal of Alloys and Compounds

journal homepage: www.elsevier.com/locate/jalcom

The effect of structural evolution on the magnetocaloric properties of Cu-added GdHoErNi high-entropy alloys

Zhongwei Pei [a,b], Hangboce Yin [b,*], Fan Chen [b], Yunshuang Ma [b], Meng Gao [b], Lijian Song [b], Yan Zhang [b], Wei Xu [b], Jun-Qiang Wang [b,*], Juntao Huo [b,*]

[a] School of Materials Science and Chemical Engineering, Ningbo University, Ningbo 315211, China
[b] CAS Key Laboratory of Magnetic Materials and Devices, and Zhejiang Province Key Laboratory of Magnetic Materials and Application Technology, Ningbo Institute of Materials Technology and Engineering, Chinese Academy of Sciences, Ningbo 315201, China

ARTICLE INFO

Keywords:
Cu addition
High-entropy alloy
Ribbon
Cooling efficiency
Magnetocaloric effect

ABSTRACT

The $(Gd_{25}Ho_{25}Er_{25}Ni_{25})_{100-x}Cu_x$ (x = 0, 10, and 20) high-entropy alloys (HEAs) were obtained after compositional design and melt-spinning technology. The Curie temperatures of the $(Gd_{25}Ho_{25}Er_{25}Ni_{25})_{100-x}Cu_x$ (x = 0, 10, and 20) alloys are 41, 45, and 42 K, respectively, lying in the temperature range required by hydrogen liquefaction, i.e., 20–77 K. The Cu-free alloy shows an amorphous/nanocrystalline dual-phase structure with an enrichment of Ni element within the minor amorphous phase. The Cu-added alloys exhibit a fully amorphous structure with a uniform distribution of elements. The structure evolution of the studied alloys is attributed to the enhanced glass-forming ability induced by Cu-addition. These structural and compositional differences lead to a clear distinction in critical exponents near phase transitions between the Cu-free and Cu-added alloys, as well as a significantly lower peak value of magnetic entropy change for the Cu-free alloy (9.2 J kg^{-1} K^{-1} (5 T)) compared to Cu-added alloys (10.8–11.1 J kg^{-1} K^{-1} (5 T)). The Cu-added alloys possess the comparable magnetocaloric properties to those of the reported rare-earth-containing high-entropy-metallic-glasses with similar transition temperatures. The designed Cu-added GdHoErNi HEAs exhibit a great potential as high-performance magnetic refrigerants suitable for hydrogen liquefaction applications.

1. Introduction

In comparison to traditional gas compression refrigeration, magnetic refrigeration (MR) based on magnetocaloric effect (MCE) has emerged as a current research hotspot, owing to its merits such as high efficiency, stability, and environmental friendliness [1–4]. Consequently, MR is widely considered to be the next generation of refrigeration technology [5]. The key of MR technology lies in the exploration of magnetocaloric materials, which are suitable for refrigeration cycles with high MCE performance in the targeted temperature range. Sustainable hydrogen energy is a cornerstone of climate-neutrality. Hydrogen liquefaction is important for efficiently storing and transporting hydrogen energy [6,7]. Therefore, if pre-cooled by liquid nitrogen, it is of great significance to explore magnetocaloric materials working in the temperature range required by hydrogen liquefaction, i.e., 20–77 K [7].

In recent years, materials with giant MCE, e.g. GdSiGe [8], LaFeCoSi [9], MnFePAs [10], and NiMnGa [11], have been developed. The high magnetic entropy changes ($|\Delta S_M|$) of these materials are attributed to their first-order magnetic transitions (FOMT). However, the noticeable magnetic and thermal hysteresis induced by FOMT, and narrow working temperature span hinder the application of these materials. In contrast, materials undergoing second-order magnetic transitions (SOMT) exhibit comparable MCE properties, negligible magnetic and thermal hysteresis, and broad working temperature spans [12]. Therefore, SOMT materials have attracted considerable attention recently. Among the SOMT materials, rare-earth (RE) containing alloys show the relatively high $|\Delta S_M|$, which is ascribed to the highly effective magnetic moments of the RE elements [13]. Most research related with SOMT materials focuses on the alloys with an amorphous or crystalline structure [3,13,14]. Wang et al. stated that $Gd_{34}Ni_{33}Al_{33}$ metallic glass exhibited the Curie temperature (T_C) of 38 K and peak value of magnetic entropy change ($|\Delta S_M^{pk}|$) of 11.06 J kg^{-1} K^{-1} under a magnetic field change ($\mu_0\Delta H$) of 5 T [15]. The $Er_{60}Cu_{20}Al_{20}$ amorphous alloy was explored. This alloy showed a $|\Delta S_M^{pk}|$ of 12.2 J kg^{-1} K^{-1} at $\mu_0\Delta H = 5$ T and T_C of 13.3 K [16]. The distances between magnetic atoms in amorphous alloy are longer

* Corresponding authors.
E-mail addresses: hbcyin@nimte.ac.cn (H. Yin), jqwang@nimte.ac.cn (J.-Q. Wang), huojuntao@nimte.ac.cn (J. Huo).

https://doi.org/10.1016/j.jallcom.2025.178974
Received 20 June 2024; Received in revised form 9 January 2025; Accepted 2 February 2025
Available online 3 February 2025

than those in crystalline alloys with the same compositions, which is due to the homogenous structure of amorphous alloys [17]. Non-magnetic elements like Al or Cu are often employed to enhance the glass-forming ability (GFA) of RE-containing amorphous alloys [15,16,18]. These atoms tend to occupy the positions isolating the magnetic atoms in RE-containing amorphous alloys [17]. These lead to promising applications for RE-containing amorphous alloys at cryogenic temperatures, especially in hydrogen liquefaction temperature range [3]. In addition, due to the disorder structure, the amorphous alloys possess the superior mechanical and corrosion resistance properties [19,20], making them suitable for refrigeration cycles. In the field of crystalline alloys, high-entropy alloys (HEAs), as a new class of alloy system, have been developed rapidly in recent years [4,14].

Unlike conventional alloys, HEAs involve multiple primary elements (≥ 4), providing an extensive compositional design space [21–23]. Yuan et al. [14] reported that the transition temperatures for $Tb_{25}Dy_{25}Ho_{25}Er_{25}$, $Gd_{25}Tb_{25}Ho_{25}Er_{25}$, and $Gd_{20}Tb_{20}Dy_{20}Ho_{20}Er_{20}$ alloys are 52, 139 and 186 K, respectively. The transition temperature of RE-containing alloys is commonly proportional to the deGennes factor of RE elements. Starting from Gd, the deGennes factor of elements decreases with increasing atomic number [24]. From the above results, it can be inferred that the design concept of multiple major RE elements could tune the magnetic transition temperature of the RE-containing HEA to the desired temperature range. Additionally, they found that $Gd_{20}Tb_{20}Dy_{20}Ho_{20}Er_{20}$ alloy exhibited the relatively high $|\Delta S_M^{pk}|$ of 8.6 J kg^{-1} K^{-1}, wide working temperature span, and resultant high refrigerant capacity (*RC*) of 627 J kg^{-1} at $\mu_0\Delta H = 5$ T. The high mixing entropy (ΔS_{mix}) in HEAs leads to chemical disorder, hindering the ordered arrangement of magnetic moments, thus causing slow rotation of magnetic moments during the phase transition. This broadens their working temperature span and enhances the MCE properties.

As a combination of RE-containing amorphous alloys and HEAs, RE-containing high-entropy-metallic-glasses (HE-MGs) exhibit both strong topological and chemical disorder, leading to improved MCE properties [4,25,26]. We [25] prepared the RE-containing HE-MGs with the compositions of $Gd_{20}Tb_{20}Dy_{20}Al_{20}TM_{20}$ (TM = Co, Ni, and Fe). These alloys showed the $|\Delta S_M^{pk}|$ in the range of 5.96–9.43 J kg^{-1} K^{-1} and *RC* in the range of 507–691 J kg^{-1} at $\mu_0\Delta H = 5$ T. However, it is unclear how the structure of HE-MGs contributes to the enhancement of the MCE performance. To address this issue, it is necessary to prepare RE-containing HE-MGs with different structures. The GFA is affected by atomic size difference (δ), ΔS_{mix}, and mixing enthalpies (ΔH_{mix}). The enhancement of GFA is favored by larger δ, higher ΔS_{mix}, and higher absolute values of negative ΔH_{mix} compared to solid solution alloys [27].

We noticed that Gd, Ho, and Er elements exhibit the relatively high magnetic moments [28]. In addition, the deGennes factor of Gd differs significantly from that of Ho and Er. Therefore, when these elements are all major constituents, according to the rule of mixture, it is highly probable that the working temperature range of the alloy would be within the temperature range required by hydrogen liquefaction (20–77 K) [29]. Based on the above compositional design principles, Zhang et al. [30] designed the HE-MG of $Gd_{20}Ho_{20}Er_{20}Ni_{20}Cu_{20}$ with T_C of 41 K and $|\Delta S_M^{pk}|$ of 12 J kg^{-1} K^{-1} at $\mu_0\Delta H = 5$ T.

The atomic size of Cu is smaller than that of RE elements. The heat of mixing for the atom pairs between Cu and RE elements are large and negative. Therefore, adding Cu in compositional design of RE-containing HEAs is beneficial for increasing their δ and the absolute value of negative ΔH_{mix}. Reducing the number of elements, such as from five to four, can decrease the ΔS_{mix} of the alloys. Mo et al. [31] and our previous work [18] found that Cu element is beneficial for enhancing the MCE properties of RE-containing alloys. Therefore, aiming to achieve the transformation of the RE-containing HEA from a crystalline or crystalline-containing structure to a fully amorphous structure, we chose to tune the Cu content in the $Gd_{20}Ho_{20}Er_{20}Ni_{20}Cu_{20}$ alloy to control its GFA.

The morphology of magnetocaloric materials significantly influences their properties and practical applications. Magnetocaloric materials typically exist in four different shapes: bulk, ribbon, microwire, and powder. Bulk materials, characterized by a small specific surface area, exhibit low heat transfer efficiency, whereas powders, despite their large specific surface area, suffer from a nonnegligible pressure drop, which limits their applicability in magnetic refrigerators [32,33]. In contrast, ribbons and microwires combine high specific surface areas with excellent mechanical strength, making them more suitable for practical cooling devices [32,33]. Recent studies have demonstrated that ribbons [12,15,16,18,26,30,34–42] and microwires [43–55], which are also applicable in chemical and environmental sciences [56], possess excellent MCE.

In this study, we designed the HEA compositions of $(Gd_{25}Ho_{25}Er_{25}Ni_{25})_{100-x}Cu_x$ (x = 0, 10, and 20). These alloys were processed into ribbon forms. The alloys without and with Cu addition show the amorphous/nanocrystalline dual-phase structure and fully amorphous structure, respectively. All elements are evenly distributed, except for the enrichment of Ni in the minor amorphous phase of the Cu-free alloy. The T_C of the studied alloys are in the temperature range of 41–45 K. Compared with the Cu-free alloy, the Cu-added alloys exhibit the higher $|\Delta S_M^{pk}|$, i.e., 10.8–11.1 J kg^{-1} K^{-1} at $\mu_0\Delta H = 5$ T. The Cu-added alloys exhibit the comparable magnetocaloric properties to those of the reported RE-containing HE-MGs with the similar transition temperatures.

2. Experimental details

The master alloys with the nominal compositions of $(Gd_{25}Ho_{25}Er_{25}Ni_{25})_{100-x}Cu_x$ (x = 0, 10, and 20) were prepared by arc melting the mixtures of commercial-grade metals with purities higher than 99.9 wt%. These alloys are hereafter referred to as Cu0, Cu10, and Cu20, respectively. This fabrication procedure was performed under a Ti-gettered argon atmosphere. To achieve high chemical uniformity, each pre-alloyed ingot was remelted five times. After the arc melting process, the mass losses of the ingots were less than 0.5 %. Subsequently, the ingots were put into the melt-spinning equipment. The alloy ribbons were obtained by dropping the melt onto a spinning Cu roller with a surface velocity of 45 m/s. The thicknesses of Cu0, Cu10 and Cu20 ribbons are about 47, 29, and 25 μm, respectively. The structure of the ribbons was preliminarily examined by an X-ray diffraction (XRD, Bruker D8 Advance) over a 2θ range of 20° to 80°. The thermal analysis for the ribbons was carried out by a differential scanning calorimetry (DSC) from room temperature to 1250 K at a heating rate of 40 K min^{-1} (Netzsch DSC-404-C). The transmission electron microscopy (TEM, Thermo Fisher Talos F200x) equipped with energy-dispersive X-ray spectroscopy (EDS) was used to observe the nanoscale microstructure of the ribbons. The magnetic and magnetocaloric behavior was determined by a Magnetic Property Measurement System (MPMS, Quantum Design SQUID-VSM). The field-cooled (FC) and zero-field-cooled (ZFC) magnetization (*M*)-temperature (*T*) curves were tested under a magnetic field of 0.02 T. The measurements of the isothermal *M-H* curves were conducted from 100 K to 10 K. Each curve was measured from 0 to 5 T. The interval of the test temperature was 5 K.

3. Results and discussion

Fig. 1 shows the XRD patterns for Cu0, Cu10 and Cu20 alloys. The XRD pattern for Cu0 alloy exhibits the clearly sharp Bragg peaks, indicating the presence of crystalline phase. The structure of the crystalline phase is confirmed as hexagonal close-packed (HCP). The broad and diffused peaks of the Cu10 and Cu20 alloys indicate the fully amorphous structure of these alloys.

The DSC curves for Cu0, Cu10 and Cu20 alloys are displayed in Fig. 2. The exothermic peaks on all DSC curves in the temperature range

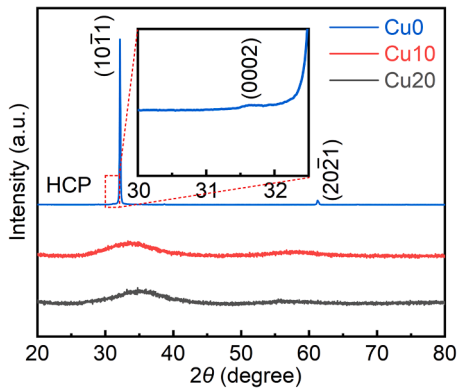

Fig. 1. XRD patterns for the Cu0, Cu10 and Cu20 alloys.

of 500–650 K confirm the crystallization of the amorphous phase for all alloys, as shown in Fig. 2a. This determines the existence of the amorphous phase for all studied alloys. The DSC curves for Cu10 and Cu20 alloys possess the endothermic peaks in the temperature range of 500–600 K, corresponding to the glass transition region. As shown in Fig. 2b, all curves exhibit the melting region, i.e., endothermic peaks in the temperature range above 950 K. The glass transition temperature (T_g), crystallization temperature (T_x), and liquidus temperature (T_l) are labeled in Fig. 2 and listed in Table 1. The absence of endothermic peaks in the temperature range below T_x results in T_g not being identifiable in the DSC curve of Cu0 alloy. The criteria for GFA, i.e., the reduced glass transition temperature (T_{rg}) and parameter γ, can be obtained as follows: $T_{rg} = T_g/T_l$ [57,58], and $\gamma = T_x/(T_g+T_l)$ [59], respectively. The width of supercooled liquid region (ΔT_x) is calculated as $\Delta T_x = T_x - T_g$ [34], which reflects the ability for hindering the crystallization of the amorphous alloy. Table 1 shows the T_{rg}, γ, and ΔT_x of Cu10 and Cu20 alloys. The T_{rg}, γ, and ΔT_x of Cu10 and Cu20 alloys are relatively high compared with those of reported MCE amorphous alloys [35–38]. Guo et al. proposed a criterion for HE-MG, i.e., $\delta \geq 9$, $-49 \leq \Delta H_{mix} \leq -5.5$ kJ mol^{-1} and $7 \leq \Delta S_{mix} \leq 16$ J K^{-1} mol^{-1} [27]. As listed in Table 1, these parameters for the Cu0, Cu10 and Cu20 alloys are in accordance with this criterion. With increasing Cu content, the absolute values of δ, ΔS_{mix}, and ΔH_{mix} increase, resulting in the relatively high GFA of Cu10 and Cu20 alloys.

TEM observations were used for analyzing the nanoscale microstructures of Cu0, Cu10, Cu20 alloys. The bright-field TEM image shows the numerous nanocrystals existing in the Cu0 alloy, as shown in Fig. 3a. The high-resolution TEM (HRTEM) image, Fig. 3b, confirms the amorphous/nanocrystalline dual-phase structure of the Cu0 alloy. This explains that the crystallization of the amorphous phase leads to the exothermic peak of the Cu0 alloy in Fig. 2a. Fig. 3c displays the fast Fourier transform (FFT) result corresponding to the red dashed squares in Fig. 3b. The HCP structure of the nanocrystalline phase in the Cu0 alloy is determined by its FFT result and diffraction rings in the selected area electron diffraction (SAED) pattern shown in Fig. 3d. The absence of information regarding the amorphous phase structure in the XRD results of the Cu0 alloy may be attributed to the limitations of the XRD equipment in detecting phases with low fractions [44]. The absence of T_g in the DSC curve of Cu0 alloy is a common phenomenon in the DSC curves of the amorphous/nanocrystalline dual-phase alloys [60,61]. The HRTEM images of Cu10 and Cu20 alloys (Fig. 3e and f) show the homogeneous maze-like patterns. In the insets of Fig. 3e and f, the SAED patterns exhibit the rather faint and diffused halo rings without any noticeable diffraction spot. These results confirm the fully amorphous structure of Cu10 and Cu20 alloys [62], in agreement with the analysis results of their XRD and DSC results. We successfully tune the structure of RE-containing HEA from crystalline-containing structure to fully amorphous structure through the compositional design. The fully amorphous structure of Cu10 and Cu20 alloys is attributed to (i) their relatively high T_{rg}, γ, and ΔT_x and (ii) their much smaller ribbon thicknesses compared with the calculated critical section thickness ($Z_c = 2.80 \times 10^{-7} \exp(41.70 \times \gamma)$ [59]), i.e., 355 and 190 μm for Cu10 and Cu20, respectively.

Fig. 4 presents the high-angle-annular-dark-field (HAADF) images and the EDS mapping results of the Cu0, Cu10 and Cu20 alloys. In Cu0 alloy, the RE elements are uniformly dispersed, with an enrichment of Ni element within the amorphous phase. This is consistent with the compositional difference between amorphous phase and nanocrystalline phase of other RE-transition-metal-element amorphous alloys [63]. The deep eutectic compositions enhance the GFA [64]. Among the elements composing the Cu0 alloy, only RE and Ni elements can form the deep eutectic systems, thereby leading to the formation of a Ni-rich amorphous phase in the Cu0 alloy. All elements are homogeneously distributed in Cu10 and Cu20 alloys.

Fig. 5a displays the FC and ZFC *M-T* curves for Cu0, Cu10 and Cu20 alloys. Based on the FC *M-T* curves, the d*M*/d*T*-*T* curves for the studied alloys are calculated and shown in the inset of Fig. 5a. The T_C of the Cu0,

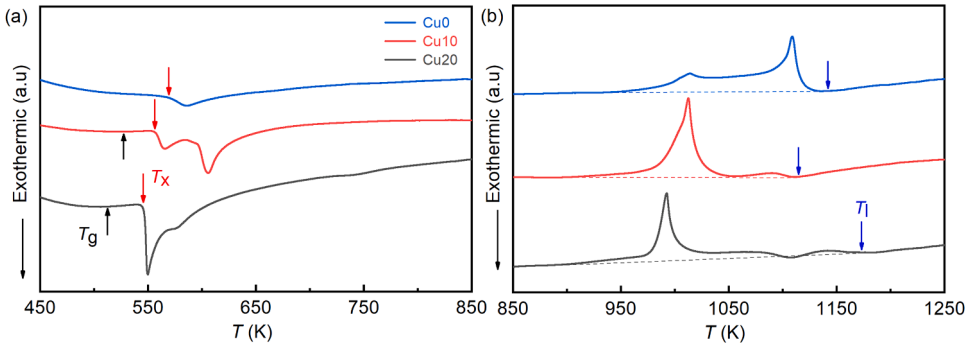

Fig. 2. DSC curves for the Cu0, Cu10 and Cu20 alloys. (a) 450–850 K; (b) 850–1250 K.

Table 1
The thermophysical parameters of the Cu0, Cu10 and Cu20 alloys.

Sample	T_g (K)	T_x (K)	T_l (K)	ΔT_x (K)	T_{rg}	γ	δ	ΔH_{mix} (kJ mol^{-1})	ΔS_{mix} (J K^{-1} mol^{-1})
Cu0	-	569	1157	-	-	-	13.97	−24	11.53
Cu10	527	556	1114	29	0.473	0.339	15.16	−25.47	13.08
Cu20	513	546	1173	33	0.437	0.322	16.03	−26.08	13.38

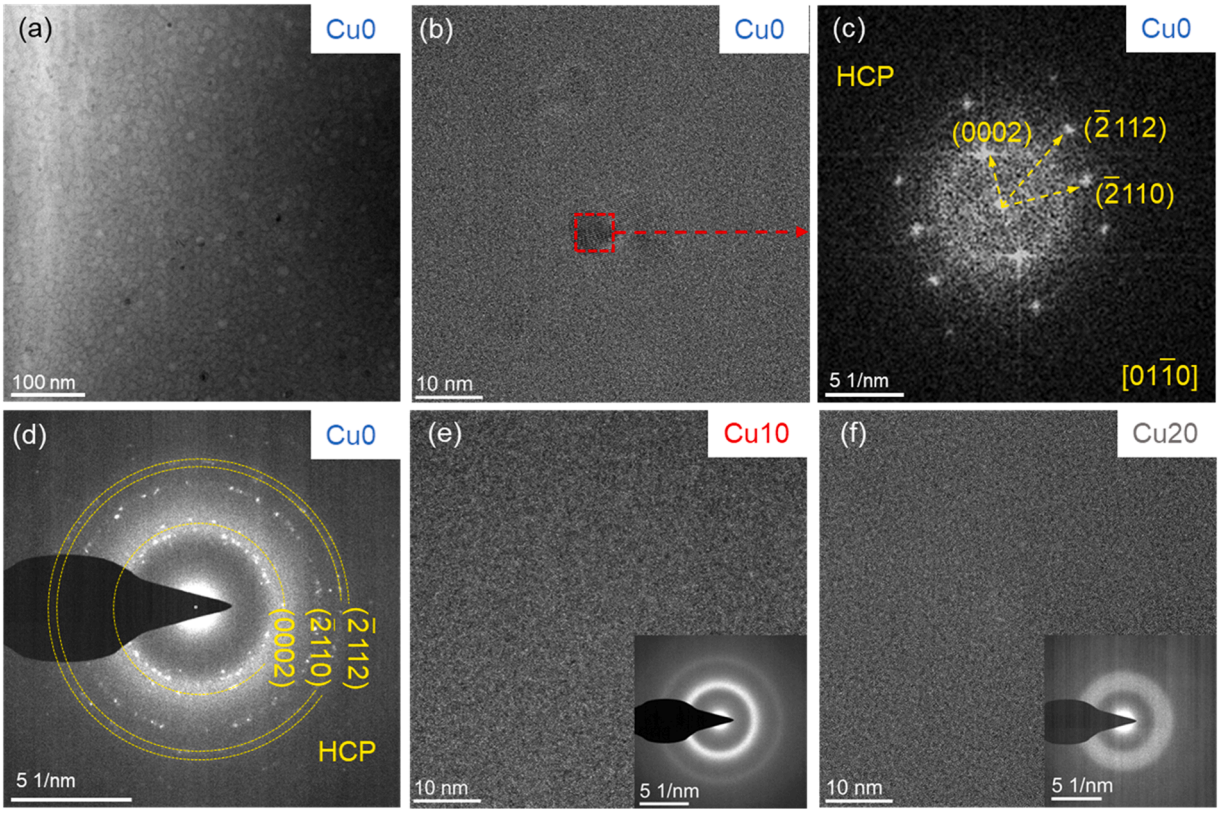

Fig. 3. (a) The bright-field TEM image of Cu0 alloy. (b) and (c) HRTEM images and FFT results corresponding to the red dashed squares in HRTEM images of Cu0 alloy, respectively. (d) the corresponding SAED results of Cu0 alloy. (e) and (f) HRTEM images and corresponding SAED results (insets) of Cu10 and Cu20 alloys, respectively.

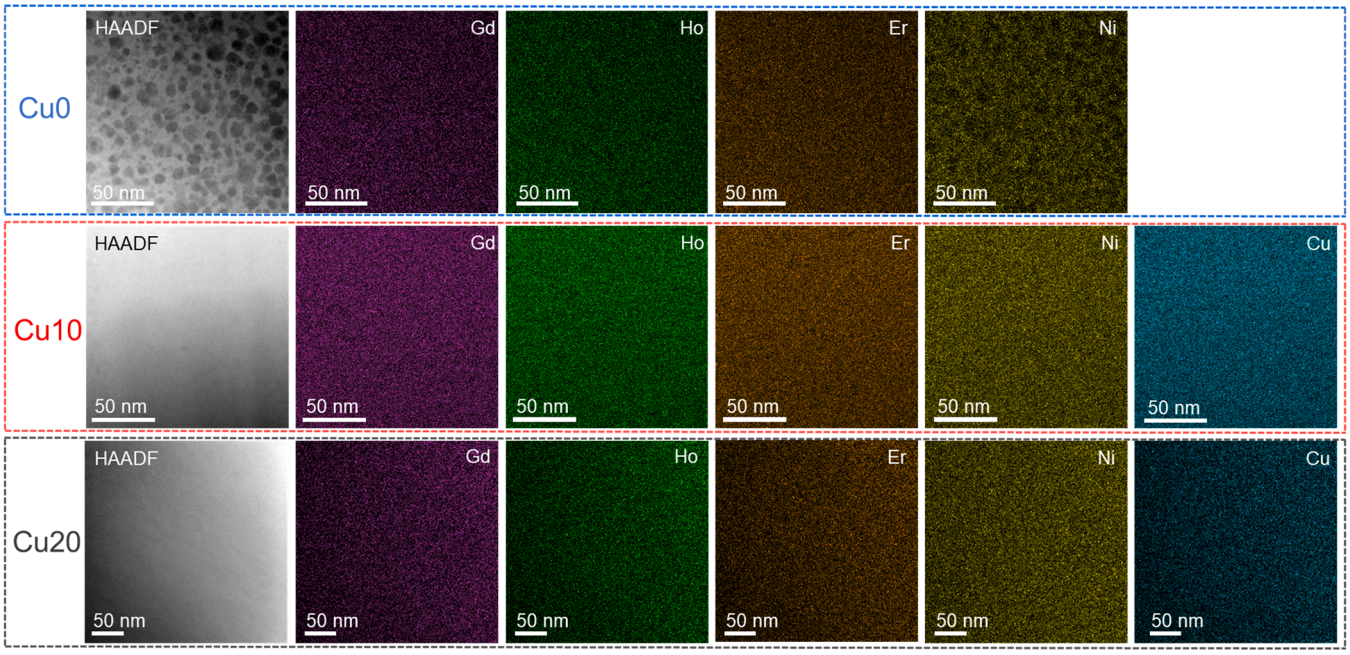

Fig. 4. The HAADF images and the EDS mapping results of the Cu0, Cu10 and Cu20 alloys.

Cu10 and Cu20 alloys is determined to be 41, 45, and 42 K, respectively, corresponding to the lowest points of the dM/dT-T curves, as shown in the inset of Fig. 5a. The T_C for Cu0, Cu10 and Cu20 alloys is similar, which may be attributed to minimal impact of Cu addition on the T_C of the RE-containing alloys [31,65]. The FC and ZFC M-T curves of the studied alloys exhibit a distinct divergence at low temperature, indicating the typical spin-glass behavior [66–68]. In the spin-glass state, the magnetic moments are more difficult to rotate compared to those in the ferromagnetic state [26,39]. Therefore, the presence of the spin-glass phase can effectively broaden the working temperature span of

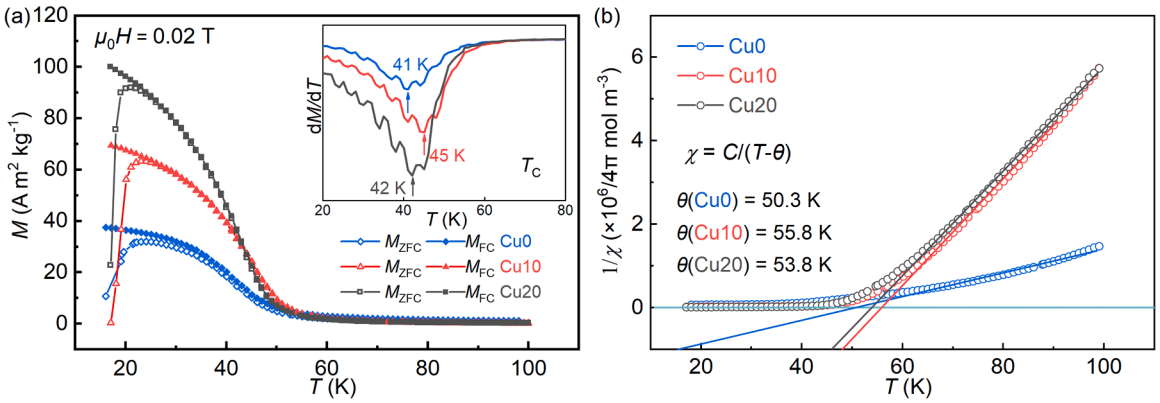

Fig. 5. (a) ZFC and FC *M-T* curves for Cu0, Cu10 and Cu20 alloys under a magnetic field of 0.02 T. The inset shows the d*M*/d*T*-*T* curves. (b) Temperature dependence of the inverse magnetic susceptibility and the linear fit for Cu0, Cu10 and Cu20 alloys.

magnetocaloric materials. The inverse magnetic susceptibility, i.e., $\chi^{-1} = \mu_0 H/M$, derived from the *M-T* curves is presented in Fig. 5b. By fitting the linear portion of the χ^{-1}-*T* curves, the obtained Curie-Weiss temperature (θ_p) are $\theta_{p1} = 50.3$ K, $\theta_{p2} = 55.8$ K, and $\theta_{p3} = 53.8$ K, for Cu0, Cu10 and Cu20 alloys, respectively. The effective magnetic moment (μ_{eff}) can be obtained by [47]: $\mu_{eff} = \sqrt{8C}\mu_B$, where *C* is Curie constant. Based on the fitted straight lines, we obtained $\mu_{eff} = 16.85\ \mu_B$, 7.90 μ_B, and 8.02 μ_B for the Cu0, Cu10 and Cu20 alloys, respectively. The μ_{eff} of Cu0 alloys is significantly larger than that of Cu10 and Cu20 alloys because Cu0 alloy contains intermetallic compounds rather than being simply amorphous [17]. For the Cu10 and Cu20 alloys, the μ_{eff} increase with the addition of Cu. This increase is attributed to the reduction of antiferromagnetic exchange interactions between the 3*d* transition metal elements and the 4 *f* rare earth elements (Ni and RE, RE = Gd, Ho, Er) caused by the addition of the nonmagnetic element Cu, leading to the observed increase in μ_{eff} [47].

Fig. 6 shows the isothermal *M*-$\mu_0 H$ curves of Cu0, Cu10 and Cu20 alloys. At high temperature range, the magnetization increases linearly with the increase of applied magnetic field, indicating the paramagnetic state of the studied alloys. The ferromagnetic state of Cu0, Cu10 and Cu20 alloys at low temperatures is confirmed by a rapid increase in magnetization with increasing applied magnetic field, followed by a saturation. As the temperature decreases, the studied alloys possess the paramagnetic-ferromagnetic (PM-FM) transition.

To determine the magnetic transition types of Cu0, Cu10 and Cu20 alloys, Arrott plots were obtained based on the *M*-$\mu_0 H$ curves, as shown in Fig. 7. According to the Banerjee criterion [69], as the slope of the Arrott plots is negative, the magnetic transition type is identified as a FOMT. Conversely, the SOMT can be confirmed by the positive slope of Arrott plots. All Arrott plots for Cu0, Cu10 and Cu20 alloys show positive slopes, suggesting the presence of SOMT in these alloys. Due to the limitation of the Arrott plots in determining magnetic transition types of MCE materials [70], additional methods have been applied to analyze magnetic transition types of the studied alloys. The relevant results are presented in the subsequent sections. According to the Maxwell relation, the ΔS_M of magnetic materials can be obtained based on the isothermal *M*-$\mu_0 H$ curves and the integral method [13]:

$$\Delta S_M = \mu_0 \int_0^{H_{max}} (\partial M/\partial T) dH = \mu_0 \left(\int_0^{H} M(T_i, H) dH - \int_0^{H} M(T_{i+1}, H) dH \right) \Big/ (T_i - T_{i+1}) \quad (1)$$

where $\mu_0 H_{max}$ is the maximum value of the applied magnetic field. Fig. 8 shows the $|\Delta S_M|$ as a function of temperature at various $\mu_0 \Delta H$ for Cu0, Cu10 and Cu20 alloys. As shown in Fig. 8a-c, the $|\Delta S_M^{pk}|$ is 9.2, 10.8, and 11.1 J kg^{-1} K^{-1} for Cu0, Cu10 and Cu20 alloys, respectively, at $\mu_0 \Delta H = 5$ T. The $|\Delta S_M^{pk}|$ of Cu20 alloy is close to that of the reported alloy with the same composition, i.e., 12 J kg^{-1} K^{-1} at $\mu_0 \Delta H = 5$ T [30]. In addition, all $|\Delta S_M|$-*T* curves show the working temperature ranges covering the temperature range of 20–77 K. This indicates success of our compositional design for the RE-containing HE-MG working in the temperature range required by hydrogen liquefaction. Fig. 8d displays the $|\Delta S_M|$-*T* curves of Cu0, Cu10 and Cu20 alloys at $\mu_0 \Delta H = 5$ T. The Cu10 and Cu20 alloys possess the similar and relatively high $|\Delta S_M|$ compared with that of Cu0 alloy. The addition of Cu gradually increases the $|\Delta S_M^{pk}|$. This increase in isothermal $|\Delta S_M|$ arises from the interplay between the competition of ferromagnetic (FM) and antiferromagnetic (AFM) exchange interactions among the elements and the magnetic dilution effect of Cu [47,52]. As a non-magnetic element, Cu increases the RE-RE (RE = Gd, Ho, Er) distance when incorporated into the alloy, thereby diluting the FM RE-RE exchange interactions [52]. With increasing Cu content, the Ni content decreases, leading to a reduction in the RE-Ni AFM interactions. These result in an increase in the $|\Delta S_M^{pk}|$ with higher Cu content [47,52]. In addition, the adiabatic temperature change (ΔT_{ad}) under a magnetic field variation can be determined

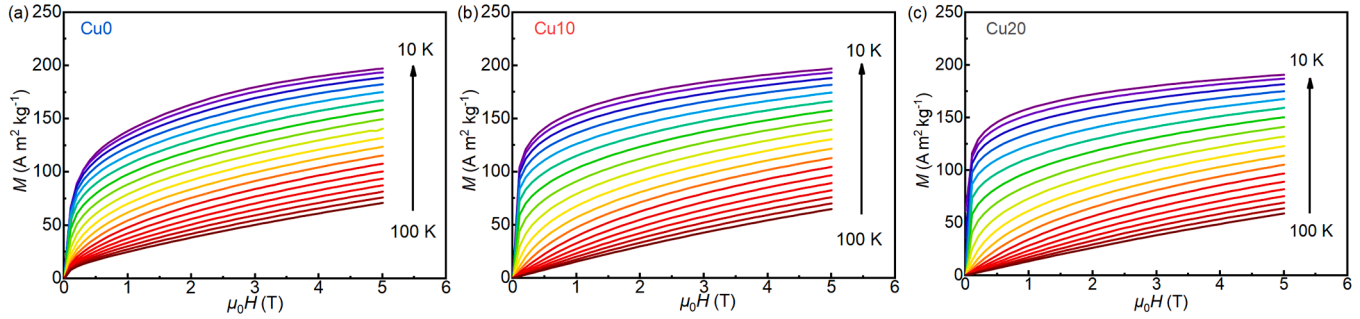

Fig. 6. Isothermal *M*-$\mu_0 H$ curves at 0–5 T. (a) Cu0; (b) Cu10; (c) Cu20.

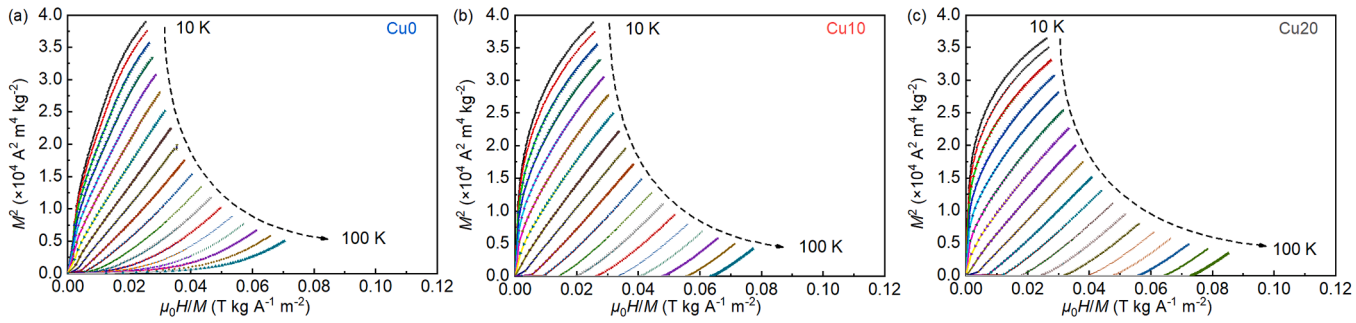

Fig. 7. Arrott plots obtained based on isothermal M-μ_0H curves. (a) Cu0; (b) Cu10; (c) Cu20.

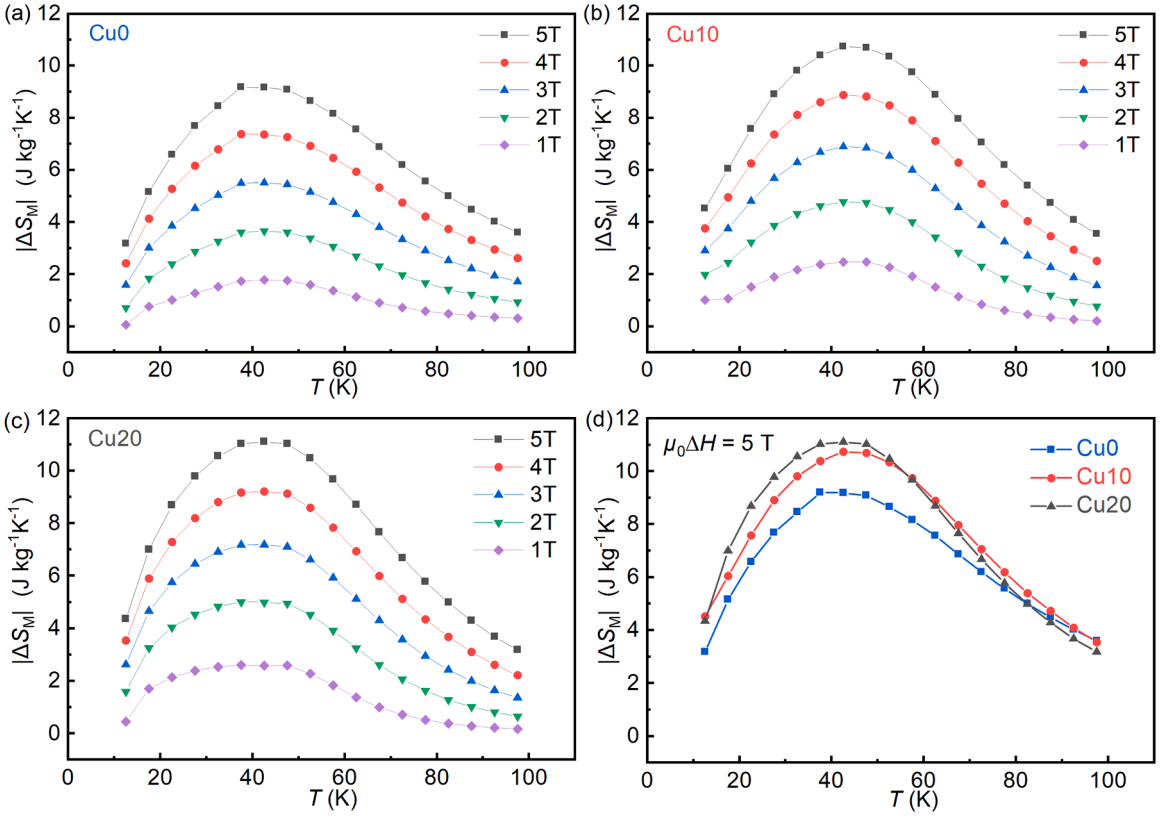

Fig. 8. $|\Delta S_M|$-T curves of (a) Cu0, (b) Cu10, and (c) Cu20 alloys at $\mu_0\Delta H$ = 1–5 T. (d) $|\Delta S_M|$-T curves for all studied alloys at $\mu_0\Delta H$ = 5 T.

indirectly from the measured magnetization and the temperature dependence of heat capacity ($C_p(T)$) at 0 T [71]:

$$\Delta T_{ad}(T,H) = T/C_p(T) * \Delta S_M(T,H) \quad (2)$$

By this method, the ΔT_{ad} of the Cu20 alloy under field changes of 1 T, 2 T, 3 T, 4 T and 5 T is shown in Fig. 9, the inset of which shows the temperature dependence of heat capacity at 0 T. The maximum values of ΔT_{ad} are determined to be 0.83, 1.59, 2.29, 2.95 and 3.59 K under field changes of 1, 2, 3, 4 and 5 T, respectively. These values are comparable to previously reported Gd-based MG [72].

In addition to ΔS_M and ΔT_{ad}, another key parameter for evaluating the MCE properties is cooling efficiency, indirectly quantifying the amount of heat transferred in an ideal refrigeration cycle. The widely used cooling efficiency parameters are relative cooling power (*RCP*) and refrigeration capacity (*RC*) [73]. These parameters can be obtained as follows:

$$RCP = \left|\Delta S_M^{pk}\right| \times \Delta T_{FWHM} = \left|\Delta S_M^{pk}\right|(T_2 - T_1) \quad (3)$$

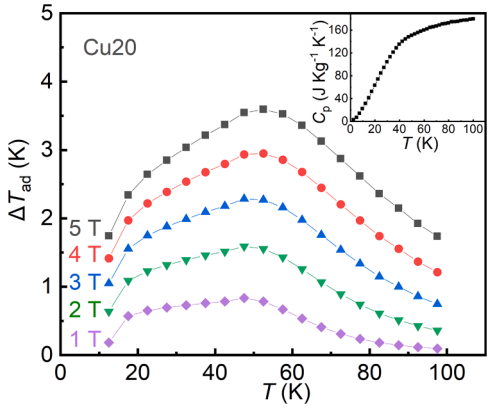

Fig. 9. The adiabatic temperature change under field changes of 1 T, 2 T, 3 T, 4 T and 5 T for the Cu20 alloy measured at temperatures between 10 and 100 K. The inset shows the temperature dependence of heat capacity at 0 T.

$$RC = \int_{T_1}^{T_2} |\Delta S_M(T)| dT \quad (4)$$

where T_1 and T_2 represent the initial and final temperatures, respectively, corresponding to the full-width at half-maximum of the $|\Delta S_M|$-T curve (ΔT_{FWHM}), i.e., working temperature span. The magnetocaloric parameters for Cu0, Cu10 and Cu20 alloys are listed in Table 2. The ΔT_{FWHM} for the Cu0, Cu10 and Cu20 alloys is 70.4 K, 67.5 K, and 64.2 K, respectively. The strong competition between FM and AFM interactions and spin-glass phase results in the largest ΔT_{FWHM} for Cu0 [47]. While the addition of Cu in Cu10 and Cu20 reduces AFM interactions, the competition between FM and AFM still exists, leading to relatively large ΔT_{FWHM}. However, the higher $|\Delta S_M|$ of Cu10 and Cu20 compensates for their smaller ΔT_{FWHM}, resulting in their relatively large RC.

The formula of $|\Delta S_M| \propto (\mu_0 \Delta H)^n$ is commonly used to describe to the relationship between $|\Delta S_M|$ and $\mu_0 \Delta H$ [74]. Exponent n is simultaneously related to the temperature and magnetic field change. The local value of exponent n can be obtained by the following equation:

$$n = d\ln|\Delta S_M| / d\ln|\mu_0 \Delta H| \quad (5)$$

Fig. 10a shows the n-T curves at $\mu_0 \Delta H = 5$ T for Cu0, Cu10 and Cu20 alloys. In the whole temperature range, all n-T curves are below 2, confirming the SOMT of Cu0, Cu10 and Cu20 alloys [75,76]. The presence of only one phase transition feature in the $|\Delta S_M|$-T and n-T curves of Cu0 alloy, as shown in Fig. 8a and d, and Fig. 10a, may be attributed to its amorphous phase with low fraction [77].

The rescaled curve is another widely used method to analyze the magnetic transition type of the MCE materials [75,78]. Based on the $|\Delta S_M|$-T curves, the y-axis of the rescaled curves is obtained by $\Delta S_M / \Delta S_M^{pk}$. The temperature of the magnetocaloric curves is normalized to a dimensionless axis (θ), i.e., x-axis of the rescaled curves, by the following equation [74]:

$$\theta = \begin{cases} -(T - T_{peak}) / (T_{r1} - T_{peak}); & T \text{ and } T_{r1} \le T_{peak} \\ (T - T_{peak}) / (T_{r2} - T_{peak}); & T \text{ and } T_{r2} > T_{peak} \end{cases} \quad (6)$$

where T_{peak} represents the temperature corresponding to $|\Delta S_M^{pk}|$, T_{r1} and T_{r2} represent reference temperatures corresponding to $\Delta S_M(T_{r1}) = \Delta S_M(T_{r2}) = 0.7 \Delta S_M^{pk}$. Fig. 10b-d show the rescaled curves of the Cu0, Cu10 and Cu20 alloys at $\mu_0 \Delta H = 2$-5 T, respectively. The rescaled curves for Cu10 alloy collapse well onto a single universal curve, confirming the SOMT in this alloy [75]. For Cu0 and Cu20 alloys, although there is relatively poor overlap in their rescaled curves, the degree of dispersion is within the acceptable range of using the rescaled curves to determine the SOMT [70]. Therefore, both Cu0 and Cu20 alloys exhibit SOMT within the test temperature range.

The $\mu_0 \Delta H$ dependence of $|\Delta S_M^{pk}|$ follows the power-law relationship [79]:

Table 2
The T_C, $|\Delta S_M^{pk}|$, and RC at $\mu_0 \Delta H = 5$ T for Cu0, Cu10, Cu20 alloys, and reported RE-containing HE-MGs working in hydrogen liquefaction temperature.

Sample	T_C (K)	$\mu_0 \Delta H$ (T)	$\lvert\Delta S_M^{pk}\rvert$ (J kg^{-1} K^{-1})	RC (J kg^{-1})	Refs.
Cu0	41	5	9.2	518	This work
Cu10	45	5	10.8	585	This work
Cu20	42	5	11.1	585	This work
$Gd_{20}Ho_{20}Er_{20}Ni_{20}Cu_{20}$	41	5	12	640.8	[30]
$Dy_{36}Ho_{20}Al_{24}Co_{20}$	23	5	9.49	326	[93]
$Gd_{18}Ho_{22}Tm_{20}Cu_{22}Al_{18}$	33.6	5	8.7	401.8	[40]
$Gd_{25}Co_{25}Al_{25}Ho_{20}Y_5$	49	5	8.79	547	[41]
$Gd_{20}Tb_{20}Dy_{20}Al_{20}Ni_{20}$	45	5	7.25	507	[25]
$Er_{20}Dy_{20}Co_{20}Al_{20}Tb_{20}$	29	5	8.6	525	[67]
$Gd_{20}Ho_{20}Er_{20}Al_{20}Ni_{20}$	25	5	9.5	511	[94]
$Sm_{20}Gd_{20}Dy_{20}Co_{20}Al_{20}$	52	5	6.34	322.9	[95]
$Gd_{20}Ho_{20}Tm_{20}Cu_{20}Ni_{20}$	32	5	10.6	528	[42]

$$\left|\Delta S_M^{pk}\right| = a(\mu_0 \Delta H)^b \quad (7)$$

where a and b represent constants. Fig. 11 shows the $|\Delta S_M^{pk}|$-$\mu_0 \Delta H$ curves and the fitting results by using Eq. (7). The results of exponent b and determination coefficients of the fitting (R^2) are listed in Table 3. The values of R^2 close to 1 indicate the good fitting. This indicates that all studied alloys exhibit SOMT [74,80], which is consistent with the analysis results of the n-T curves, rescaled curves, and Arrott plots. Both n around T_C and exponent b for alloys with SOMT are associated with the critical exponents [75,79,81]. As shown in Fig. 10a and Table 3, the n around T_C and exponent b for Cu10 and Cu20 alloys are close, which are lower than those of Cu0 alloy. This indicates the critical behavior of Cu0 alloy is different from that of Cu10 and Cu20 alloys. Due to the absence of Ni elements, there is a significant difference in composition between the nanocrystalline phase of the Cu0 alloy and the amorphous phases of the Cu10 and Cu20 alloys. This, combining the structural difference between nanocrystalline and amorphous phases, leads to a significant disparity in the critical exponents between the nanocrystalline phase of the Cu0 alloy and the amorphous phases of the Cu10 and Cu20 alloys [47,52,82,83]. The critical exponents of the amorphous phases for RE-containing HE-MGs are insensitive to compositional changes [82]. Therefore, Cu10 and Cu20 alloys with fully amorphous structures possess the similar critical exponents.

In SOMT materials, the critical behavior of the FM-PM phase transition is characterized by three critical exponents, β, γ, and δ [84], which are correlated with the magnetocaloric behavior of SOMT materials [52,85–87]. These exponents are associated with the spontaneous magnetization $M_S(T)$, the thermal dependence of the initial inverse susceptibility $\chi_0^{-1}(T)$, and the field dependence of the magnetization of the critical isotherm, respectively [84]. Their values can be defined by using the following power-law relations:

$$M_S(T) = M_0(-\varepsilon)^\beta; \ \varepsilon < 0, \ T < T_C \quad (8)$$

$$\chi_0^{-1}(T) = (H_0/M_0)\varepsilon^\gamma; \ \varepsilon > 0, \ T > T_C \quad (9)$$

$$H = DM^\delta; \ \varepsilon = 0, \ T = T_C \quad (10)$$

where ε is the reduced temperature, $\varepsilon = (T - T_C)/T_C$, and H_0, M_0, D are the critical amplitudes.

According to the Arrott-Noakes equation of state [88]:

$$(H/M)^{1/\gamma} = A\varepsilon + BM^{1/\beta} \quad (11)$$

where A and B are material dependent parameters, the T_C for all alloys can be redefined by using modified Arrott plot (MAP) method. To use MAP approach, the M-$\mu_0 H$ data is reformulated, using initial values of β and γ and according to the Eq. (11). The accurate critical exponents are those that result in a linear relationship between and $M^{1/\beta}$ and $(\mu_0 H/M)^{1/\gamma}$, with T_C determined from the critical isotherm intersecting the origin. The initial values of β and γ can be estimated using one of the four theoretical models: the mean-field model, i.e., $\beta = 0.5$, $\gamma = 1.0$, the 3D Heisenberg model, i.e., $\beta = 0.365$, $\gamma = 1.336$, the 3D Ising model, i.e., $\beta = 0.325$, $\gamma = 1.240$, and the tricritical mean field model, i.e., $\beta = 0.25$, $\gamma = 1$ [89,90]. The $M_S(T)$ and the $\chi_0^{-1}(T)$ were determined from the intercepts obtained by linearly extrapolating $M^{1/\beta}$ and $(\mu_0 H/M)^{1/\gamma}$, respectively, using the high field isotherms of the MAPs. The critical exponents β and γ are obtained by fitting $M_S(T)$ data to the relation $M_S \propto (-\varepsilon)^\beta$ as described in Eq. (8) and the $\chi_0^{-1}(T)$ data to the relation $\chi_0^{-1} \propto (\varepsilon)^\gamma$ as given in Eq. (9). This process is iterated using the updated β and γ values until the isotherm passing through the origin corresponds to $T = T_C$, and the critical exponents β and γ converge to stable values. Fig. 12a-c presents the MAPs, in which the isotherms achieve good linearity with $\beta_{MAP} = 0.641 \pm 0.003$, 0.614 ± 0.004, 0.566 ± 0.005, $\gamma_{MAP} = 1.428 \pm 0.005$, 1.381 ± 0.003, 1.370 ± 0.003, and $T_{C\text{-}MAP}$

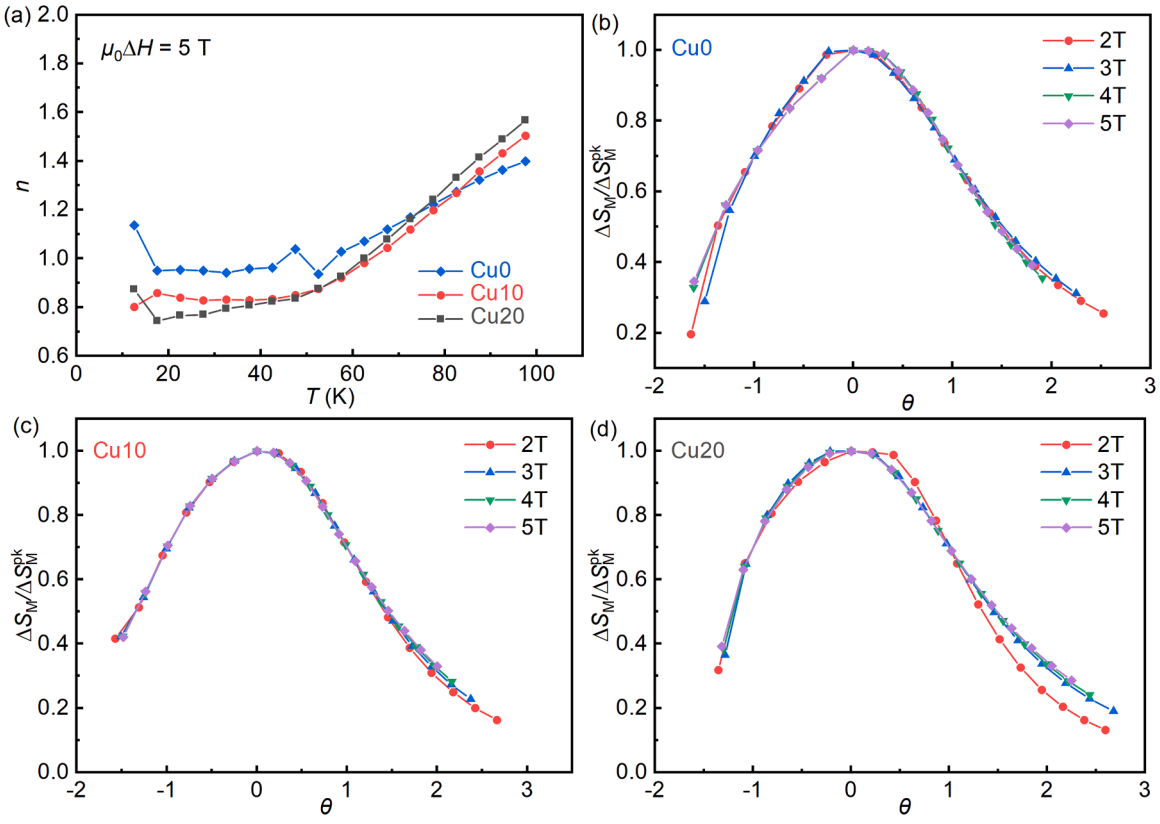

Fig. 10. (a) The n-T curves at $\mu_0\Delta H = 5$ T. The rescaled curves at $\mu_0\Delta H = 2$–5 T for the (b) Cu0, (c) Cu10, and (d) Cu20 alloys.

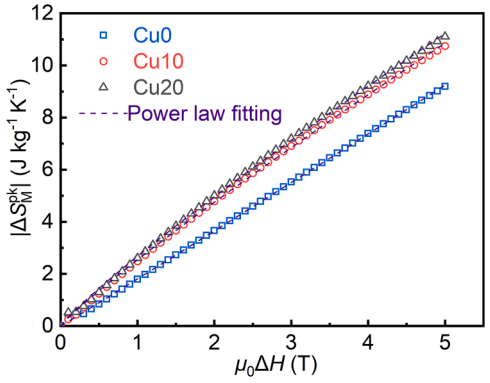

Fig. 11. The $\mu_0\Delta H$ dependence of $|\Delta S_M^{pk}|$ for Cu0, Cu10 and Cu20 alloys. The dashed lines are fitting curves.

Table 3
The exponent b and the determination coefficients of the fitting, R^2, for the Cu0, Cu10 and Cu20 alloys.

Sample	Cu0	Cu10	Cu20
b	1.01251	0.90155	0.88939
R^2	0.99987	0.99958	0.99948

= 40.74 K, 45.52 K, 43.22 K for Cu0, Cu10 and Cu20 alloys, respectively. According to the principles of statistical theory, the critical exponents β, γ and δ must satisfy the Widom scaling relation [91]:

$$\delta = 1 + \gamma/\beta \tag{12}$$

Therefore, the critical exponent δ is calculated as $\delta = 3.228 \pm 0.025$, 3.250 ± 0.005, 3.422 ± 0.003 for Cu0, Cu10 and Cu20 alloys, respectively. Furthermore, the critical exponents β, γ and δ can also be determined using the Kouvel-Fisher (KF) method by reformulating Eqs. (8) and (9) in an alternative direction [92]:

$$M_S(T)[dM_S(T)/dT]^{-1} = (T - T_C)/\beta \tag{13}$$

$$\chi_0^{-1}(T)[d\chi_0^{-1}(T)/dT]^{-1} = (T - T_C)/\gamma \tag{14}$$

In this method, $M_S(T)[dM_S(T)/dT]^{-1}$ vs. T and $\chi_0^{-1}(T)[d\chi_0^{-1}(T)/dT]^{-1}$ vs. T are plotted for all alloys on the same figures, yielding straight lines with slopes of $1/\beta$, $1/\gamma$, respectively, and intersecting the temperature axis at T_C. The exponents derived from the linear fitting are utilized to generate a revised Arrott-Noakes plot. Fig. 12d-f shows the results of $M_S(T)[dM_S(T)/dT]^{-1}$-T and $\chi_0^{-1}(T)[d\chi_0^{-1}(T)/dT]^{-1}$-$T$ and their linear fitting curves for all alloys. For temperatures below T_C, the critical exponent β is determined as $\beta_{KF} = 0.643 \pm 0.004$, 0.611 ± 0.007, 0.562 ± 0.005 with the Curie temperatures being $T_{C1} = 39.30 \pm 0.25$ K, 45.35 ± 0.35 K, 43.27 ± 0.25 K for the Cu0, Cu10 and Cu20 alloys, respectively. For temperatures above T_C, the critical exponent γ is determined as $\gamma_{KF} = 1.415 \pm 0.009$, 1.374 ± 0.005, 1.373 ± 0.010, with the Curie temperatures identified as $T_{C2} = 41.20 \pm 0.37$ K, 45.80 ± 0.30 K, 43.22 ± 0.20 K for the Cu0, Cu10 and Cu20 alloys, respectively. The critical exponent δ, as defined by Eq. (12), is determined to be $\delta_{KF} = 3.201 \pm 0.026$, 3.249 ± 0.022, 3.443 ± 0.015 for the Cu0, Cu10 and Cu20 alloys, respectively. The critical exponents for all alloys, obtained using the MAP and KF methods, are presented in Table 4 for comparison. The consistency between the results derived from the two methods validates the accuracy and reliability of the obtained critical exponents. The exponent β is significantly higher than the theoretical value of the 3D Heisenberg model (0.365) and even exceeds that of the mean field model (0.5). However, the exponent γ closely matches the

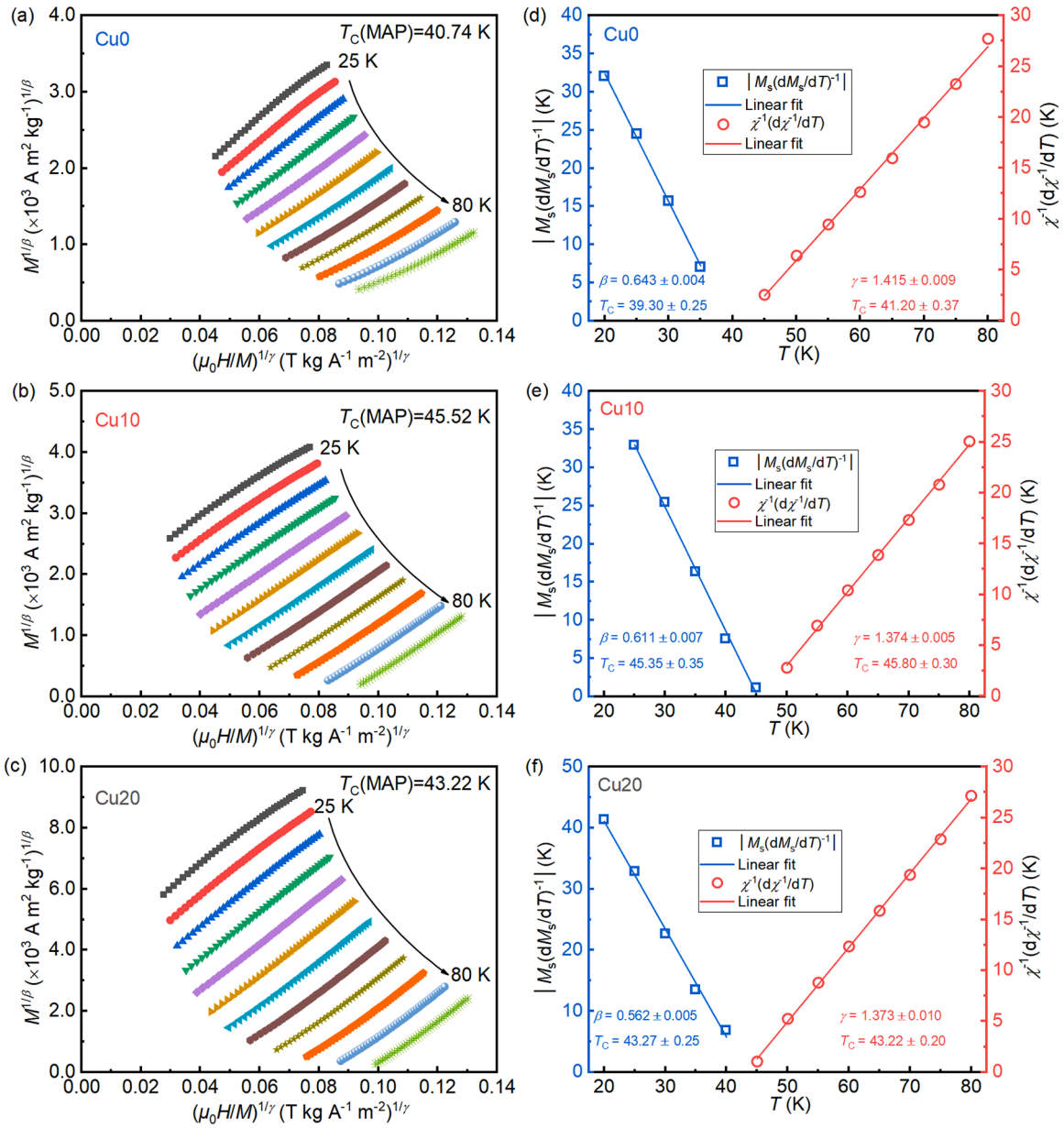

Fig. 12. (a)-(c) MAP plots of the Cu0, Cu10 and Cu20 alloys, respectively; (d)-(f) KF plots for the Cu0, Cu10 and Cu20 alloys, respectively.

theoretical value of the 3D Heisenberg model (1.336). This situation is similar to that of the reported $Gd_{60}Fe_{20}Al_{20}$ microwires [47], where the β value is relatively large, and the γ value is close to the theoretical value of the 3D Ising model. It is noteworthy that the γ values of Cu10 and Cu20 are similar, while the γ value of Cu0 is relatively higher. It is widely recognized that β characterizes the growth of the ordered moment below T_C, whereas γ describes the divergence of the magnetic susceptibility at T_C. A smaller β value indicates a more rapid growth in the ordered moment [47]. In this study, the studied alloys exhibit coexisting FM interactions between RE-RE (Gd, Ho, Er) and AFM interactions between Ni-RE (Gd, Ho, Er). The long-range behavior of FM interactions is disrupted by the AFM interactions, which break the long-range order and induce short-range ordering below T_C. Furthermore, the short-range AFM interaction exists in the nanometer-scale amorphous phase of the Cu0 alloy. These factors may result in relatively high critical exponent β values for the studied alloys, with Cu0 exhibiting the highest value. Moreover, the variation trends of n around T_C and exponent b are consistent with the γ values, indicating the effectiveness of n and b in analyzing the critical behavior near the phase transition.

Table 2 shows the magnetocaloric parameters for the studied alloys and other reported RE-containing HE-MGs working in the temperature range of 20–77 K. To visually compare the MCE properties of these alloys, the T_C dependence of $|\Delta S_M^{pk}|$ for these alloys were plotted in Fig. 13. It can be observed from this image that the Cu10 and Cu20 alloys exhibit the relatively high $|\Delta S_M^{pk}|$. The comparable MCE properties and SOMT lead to a significant potential application of Cu10 and Cu20 alloys as high-performance magnetic refrigerants within temperature range required by hydrogen liquefaction (20–77 K).

4. Conclusions

The designed Cu0, Cu10 and Cu20 alloys were prepared through melt-spinning technology. The structure of these alloys evolves form an amorphous/nanocrystalline dual-phase structure in the Cu0 alloy to a fully amorphous structure in the Cu10 and Cu20 alloys. The enhanced GFA induced by Cu addition leads to the fully amorphous structures of

Table 4
The T_C and critical exponents of the Cu0, Cu10 and Cu20 alloys in comparison with those of the theoretical models.

Material/ Model	Method	T_C (K)	β	γ	δ	Refs.
Mean field	Theory	-	0.5	1.0	3.0	[89]
3D Heisenberg	Theory	-	0.365	1.336	4.80	[89]
3D Ising	Theory	-	0.325	1.241	4.82	[89]
Tricritical mean field	Theory	-	0.25	1.0	5.0	[90]
Cu0	MAP	40.74	0.641	1.428	3.228	This work
	KF (below T_C)	39.30	0.643	-	3.201	
	KF (above T_C)	41.20	-	1.415	-	
Cu10	MAP	45.52	0.614	1.381	3.250	This work
	KF (below T_C)	45.35	0.611	-	3.249	
	KF (above T_C)	45.80	-	1.374	-	
Cu20	MAP	43.22	0.566	1.370	3.422	This work
	KF (below T_C)	43.27	0.562	-	3.443	
	KF (above T_C)	43.22	-	1.373	-	

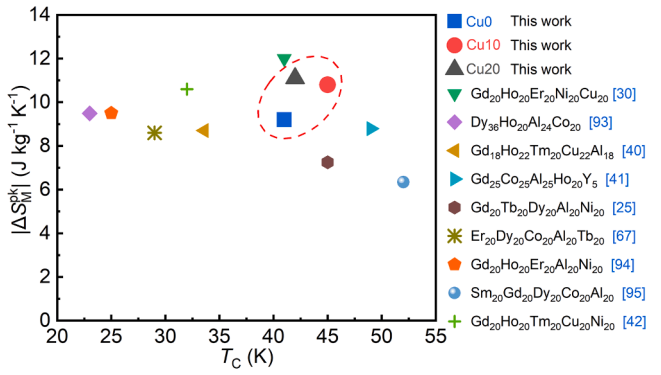

Fig. 13. The T_C dependence of $|\Delta S_M^{pk}|$ for the studied alloys and other reported RE-containing HE-MGs at $\mu_0\Delta H = 5$ T.

Cu10 and Cu 20 alloys. All studied alloys exhibit SOMT. The T_C values for the Cu0, Cu10 and Cu20 alloys are close, i.e., 41, 45, and 42 K, respectively. All studied alloys possess uniform elemental distribution, except for the Ni enrichment in the minor amorphous phase of the Cu0 alloy, leading to a significant compositional difference between nanocrystalline phase of the Cu0 alloy and the amorphous phases of the Cu10 and Cu20 alloys. This, combined with the structural difference between the Cu-free alloy and Cu-added alloys, leads to the relatively higher $|\Delta S_M^{pk}|$ values of the Cu10 and Cu20 alloys (10.8 and 11.1 J kg^{-1} K^{-1}, respectively) compared to the Cu0 alloy (9.2 J kg^{-1} K^{-1}) at $\mu_0\Delta H = 5$ T, as well as notable differences in critical exponents near phase transitions between the Cu-free and Cu-added alloys. In addition, the coexistence of AFM and FM interactions results in relatively large critical exponent β values for all the studied alloys, with Cu0 exhibiting the highest value. The Cu10 and Cu20 alloys possess the comparable MCE properties with respect to those of the reported RE-containing HE-MGs with the similar T_C, making them suitable as the high-performance magnetic refrigerants within temperature range required by hydrogen liquefaction (20–77 K).

CRediT authorship contribution statement

Chen Fan: Investigation, Formal analysis. **Ma Yunshuang:** Investigation, Formal analysis. **Gao Meng:** Project administration, Investigation, Funding acquisition. **Song Lijian:** Supervision, Project administration, Methodology, Investigation, Funding acquisition, Formal analysis. **Zhang Yan:** Supervision, Funding acquisition, Formal analysis. **Xu Wei:** Supervision, Formal analysis. **Wang Jun-Qiang:** Writing – review & editing, Supervision, Project administration, Methodology, Investigation, Funding acquisition. **Huo Juntao:** Writing – review & editing, Supervision, Project administration, Methodology, Investigation, Funding acquisition, Formal analysis. **Pei Zhongwei:** Writing – original draft, Investigation, Formal analysis. **Yin Hangboce:** Writing – review & editing, Supervision, Project administration, Methodology, Investigation, Funding acquisition, Formal analysis, Data curation.

Declaration of Competing Interest

The authors declare that they have no known competing financial interests or personal relationships that could have appeared to influence the work reported in this paper.

Acknowledgments

We acknowledge financial support from the National Key R&D Program of China (No. 2018YFA0703600), National Natural Science Foundation of China (Nos. 52222105, 51827801, 51922102, 52001319, 92163108, 52201193, 52301223), Zhejiang Provincial Natural Science Foundation of China (Nos. LGF22E010002, LZ22A030001, LR22E010004), "Pioneer and Leading Goose" R&D Program of Zhejiang (No. 2022C01023), Ningbo Key Scientific and Technological Project (No. 2019B10051), and Natural Science Foundation of Ningbo City (No. 2023J346). This research was supported by Zhejiang Provincial Natural Science Foundation of China under Grant No. LQ24E010004.

Data availability

Data will be made available on request.

References

[1] O. Tegus, E. Brück, K.H.J. Buschow, F.R. de Boer, Transition-metal-based magnetic refrigerants for room-temperature applications, Nature 415 (2002) 150–152, https://doi.org/10.1038/415150a.
[2] K.A. Gschneidner, V.K. Pecharsky, A.O. Tsokol, Recent developments in magnetocaloric materials, Rep. Prog. Phys. 68 (2005) 1479, https://doi.org/10.1088/0034-4885/68/6/R04.
[3] V. Franco, J.S. Blázquez, J.J. Ipus, J.Y. Law, L.M. Moreno-Ramírez, A. Conde, Magnetocaloric effect: from materials research to refrigeration devices, Prog. Mater. Sci. 93 (2018) 112–232, https://doi.org/10.1016/j.pmatsci.2017.10.005.
[4] J.Y. Law, V. Franco, Review on magnetocaloric high-entropy alloys: design and analysis methods, J. Mater. Res. 38 (2023) 37–51, https://doi.org/10.1557/s43578-022-00712-0.
[5] H.B. Tran, T. Fukushima, H. Momida, K. Sato, Y. Makino, T. Oguchi, Theoretical prediction of large anisotropic magnetocaloric effect in MnP, Comput. Mater. Sci. 188 (2021) 110227, https://doi.org/10.1016/j.commatsci.2020.110227.
[6] W. Liu, E. Bykov, S. Taskaev, M. Bogush, V. Khovaylo, N. Fortunato, A. Aubert, H. B. Zhang, T. Gottschall, J. Wosnitza, F. Scheibel, K. Skokov, O. Gutfleisch, A study on rare-earth Laves phases for magnetocaloric liquefaction of hydrogen, Appl. Mater. Today 29 (2022) 101624, https://doi.org/10.1016/j.apmt.2022.101624.
[7] W. Liu, T. Gottschall, F. Scheibel, E. Bykov, N. Fortunato, A. Aubert, H.B. Zhang, K. Skokov, O. Gutfleisch, Designing magnetocaloric materials for hydrogen liquefaction with light rare-earth Laves phases, J. Phys. Energy 5 (2023) 034001, https://doi.org/10.1088/2515-7655/accb0b.
[8] V.K. Pecharsky, K.A. Gschneidner, Jr, Giant magnetocaloric effect in $Gd_5(Si_2Ge_2)$, Phys. Rev. Lett. 78 (1997) 4494, https://doi.org/10.1103/PhysRevLett.78.4494.
[9] F.X. Hu, B.G. Shen, J.R. Sun, G.J. Wang, Z.H. Cheng, Very large magnetic entropy change near room temperature in $LaFe_{11.2}Co_{0.7}Si_{1.1}$, Appl. Phys. Lett. 80 (2002) 826–828, https://doi.org/10.1063/1.1447592.
[10] P. Govindappa, P.V. Trevizoli, O. Campbell, I. Niknia, T.V. Christiaanse, R. Teyber, S. Misra, M.A. Schwind, D. van Asten, L. Zhang, A. Rowe, Experimental investigation of $MnFeP_{1-x}As_x$ multilayer active magnetic regenerators, J. Phys. D: Appl. Phys. 50 (2017) 315001, https://doi.org/10.1088/1361-6463/aa7a33.
[11] A. Zhukov, V. Rodionova, M. Ilyn, A.M. Aliev, R. Varga, S. Michalik, A. Aronin, G. Abrosimova, A. Kiselev, M. Ipatov, V. Zhukova, Magnetic properties and

magnetocaloric effect in Heusler-type glass-coated NiMnGa microwires, J. Alloy. Compd. 575 (2013) 73–79, https://doi.org/10.1016/j.jallcom.2013.04.083.
[12] Q. Luo, P.N. Dinh, X.H. Kou, J. Shen, Controllable ferromagnetic/re-entrant spin glass state and magnetocaloric response of Gd-Er-Al-Co metallic glasses, J. Alloy. Compd. 725 (2017) 835–839, https://doi.org/10.1016/j.jallcom.2017.06.293.
[13] Q. Luo, W.H. Wang, Magnetocaloric effect in rare earth-based bulk metallic glasses, J. Alloy. Compd. 495 (2010) 209–216, https://doi.org/10.1016/j.jallcom.2010.01.125.
[14] Y. Yuan, Y. Wu, X. Tong, H. Zhang, H. Wang, X.J. Liu, L. Ma, H.L. Suo, Z.P. Lu, Rare-earth high-entropy alloys with giant magnetocaloric effect, Acta Mater. 125 (2017) 481–489, https://doi.org/10.1016/j.actamat.2016.12.021.
[15] X. Wang, Q. Wang, B.Z. Tang, P. Yu, L. Xia, D. Ding, Large magnetic entropy change and adiabatic temperature rise of a ternary $Gd_{34}Ni_{33}Al_{33}$ metallic glass, J. Rare Earths 39 (2021) 998–1002, https://doi.org/10.1016/j.jre.2020.04.011.
[16] J. Wang, P. Zhang, A.F. Ning, Microstructure, magnetic properties and cryogenic magnetocaloric effect in $Cu_{20}Al_{20}Er_{60}$ amorphous ribbons, J. Magn. Magn. Mater. 465 (2018) 780–783, https://doi.org/10.1016/j.jmmm.2018.05.097.
[17] G.M. Cui, X. Li, G.C. Shan, H.B. Gao, K.W. Wong, J.L. Zhang, Depression of direct exchange couplings in metallic glasses: a comparative study of critical and electronic behavior in $Gd_6Co_{4.85}$ intermetallic compound and metallic glass, Intermetallics 124 (2020) 106878, https://doi.org/10.1016/j.intermet.2020.106878.
[18] Y.S. Ma, H.B.C. Yin, F. Chen, M. Gao, L.J. Song, Y. Zhang, W. Xu, L.M. Wang, J. T. Huo, S.Z. Zhang, J.Q. Wang, Magnetocaloric effect in $(Tm_{67}Cu_{33})_{80}Al_{20}$ amorphous alloy, J. Non Cryst. Solids 604 (2023) 122151, https://doi.org/10.1016/j.jnoncrysol.2023.122151.
[19] J. Pan, Y.P. Ivanov, W.H. Zhou, Y. Li, A.L. Greer, Strain-hardening and suppression of shear-banding in rejuvenated bulk metallic glass, Nature 578 (2020) 559–562, https://doi.org/10.1038/s41586-020-2016-3.
[20] X.D. Yang, M. Gao, Y.H. Liu, J.L. Li, Y. Huang, G. Wang, J.Q. Wang, J.T. Huo, Superior corrosion resistance of high-temperature Ir–Ni–Ta–(B) amorphous alloy in sulfuric acid solution, Corros. Sci. 200 (2022) 110227, https://doi.org/10.1016/j.corsci.2022.110227.
[21] B. Cantor, I.T.H. Chang, P. Knight, A.J.B. Vincent, Microstructural development in equiatomic multicomponent alloys, Mater. Sci. Eng. A 375-377 (2004) 213–218, https://doi.org/10.1016/j.msea.2003.10.257.
[22] J.W. Yeh, S.K. Chen, S.J. Lin, J.Y. Gan, T.S. Chin, T.T. Shun, C.H. Tsau, S.Y. Chang, Nanostructured high-entropy alloys with multiple principal elements: Novel alloy design concepts and outcomes, Adv. Eng. Mater. 6 (2004) 299–303, https://doi.org/10.1002/adem.200300567.
[23] Y. Zhang, High-Entropy Materials, A Brief Introduction, Springer, Singapore, 2019, https://doi.org/10.1007/978-981-13-8526-1.
[24] K.A. Gschneidner, A.O. Pecharsky, V.K. Pecharsky, Low temperature cryocooler regenerator materials, Cryocoolers 12 (2003) 457–465, https://doi.org/10.1007/0-306-47919-2_61.
[25] J.T. Huo, L.S. Huo, H. Men, X.M. Wang, A. Inoue, J.Q. Wang, C.T. Chang, R.W. Li, The magnetocaloric effect of Gd-Tb-Dy-Al-M (M = Fe, Co and Ni) high-entropy bulk metallic glasses, Intermetallics 58 (2015) 31–35, https://doi.org/10.1016/j.intermet.2014.11.004.
[26] J.T. Huo, J.Q. Wang, W.H. Wang, Denary high entropy metallic glass with large magnetocaloric effect, J. Alloy. Compd. 776 (2019) 202–206, https://doi.org/10.1016/j.jallcom.2018.10.328.
[27] S. Guo, C.T. Liu, Phase stability in high entropy alloys: formation of solid-solution phase or amorphous phase, Prog. Nat. Sci. Mater. Inter. 21 (2011) 433–446, https://doi.org/10.1016/S1002-0071(12)60080-X.
[28] K.A. Gschneidner, Physical properties of the rare earth metals, Bull. Alloy Phase Diagr. 11 (1990) 216–224, https://doi.org/10.1007/BF03029283.
[29] Y.J. Zhao, J.W. Qiao, S.G. Ma, M.C. Gao, H.J. Yang, M.W. Chen, Y. Zhang, A hexagonal close-packed high-entropy alloy: the effect of entropy, Mater. Des. 96 (2016) 10–15, https://doi.org/10.1016/j.matdes.2016.01.149.
[30] Y.K. Zhang, D. Guo, H. Xu, Z.M. Ren, G. Wilde, Giant refrigerant capacity in equi-atomic HoErGdCuNi amorphous ribbons, J. Alloy. Compd. 792 (2019) 180–184, https://doi.org/10.1016/j.jallcom.2019.04.039.
[31] Z.J. Mo, J. Shen, G.F. Chen, L.Q. Yan, X.Q. Zheng, J.F. Wu, C.C. Tang, J.R. Sun, B. G. Shen, Evolution of magnetic properties and magnetocaloric effect in $TmNi_{1-x}Cu_xAl$ (x = 0, 0.1, 0.3, 0.5, 0.7, 0.9, 1) compounds, J. Appl. Phys. 115 (2014) 17A909, https://doi.org/10.1063/1.4861580.
[32] M.D. Kuz'min, Factors limiting the operation frequency of magnetic refrigerators, Appl. Phys. Lett. 90 (2007) 251916, https://doi.org/10.1063/1.2750540.
[33] D. Vuarnoz, T. Kawanami, Numerical analysis of a reciprocating active magnetic regenerator made of gadolinium wires, Appl. Therm. Eng. 37 (2012) 388–395, https://doi.org/10.1016/j.applthermaleng.2011.11.053.
[34] L. Xue, L.L. Shao, Q. Luo, B.L. Shen, $Gd_{25}RE_{25}Co_{25}Al_{25}$ (RE = Tb, Dy and Ho) high-entropy glassy alloys with distinct spin-glass behavior and good magnetocaloric effect, J. Alloy. Compd. 790 (2019) 633–639, https://doi.org/10.1016/j.jallcom.2019.03.210.
[35] S.L. Yu, L. Tian, J.F. Wang, X.G. Zhao, D. Li, Z.J. Mo, B. Li, Magnetic and magnetocaloric effect of $Er_{20}Ho_{20}Dy_{20}Cu_{20}Ni_{20}$ high-entropy metallic glass, Chin. Phys. B 33 (2024) 057502, https://doi.org/10.1088/1674-1056/ad1a94.
[36] Y.Y. Shu, L.F. Wang, S.L. Huang, Y.K. Zhang, Magnetic properties and large magneto-caloric effect in the amorphous $Ho_{0.2}Tm_{0.2}Gd_{0.2}Co_{0.2}Al_{0.2}$ ribbon, J. Non Cryst. Solids 628 (2024) 122846, https://doi.org/10.1016/j.jnoncrysol.2024.122846.
[37] Q. Wang, L.L. Pan, B.Z. Tang, D. Ding, L. Xia, Outstanding magnetocaloric properties at ambient temperature of a $Fe_{88}La_4Ce_3B_5$ amorphous alloy, J. Non Cryst. Solids 580 (2022) 121394, https://doi.org/10.1016/j.jnoncrysol.2021.121394.
[38] B.Z. Tang, H.X. Xie, D.M. Li, L. Xia, P. Yu, Microstructure and its effect on magnetic and magnetocaloric properties of the $Co_{50}Gd_{50-x}Fe_x$ glassy ribbons, J. Non Cryst. Solids 533 (2020) 119935, https://doi.org/10.1016/j.jnoncrysol.2020.119935.
[39] X.C. Zhong, X.W. Huang, X.Y. Shen, H.Y. Mo, Z.W. Liu, Thermal stability, magnetic properties and large refrigerant capacity of ternary $Gd_{55}Co_{35}M_{10}$ (M = Mn, Fe and Ni) amorphous alloys, J. Alloy. Compd. 682 (2016) 476–480, https://doi.org/10.1016/j.jallcom.2016.04.307.
[40] Z.Q. Dong, Z.J. Wang, S.H. Yin, Magnetic properties and magneto-caloric effect (MCE) in $Cu_{22}Al_{18}Ho_{22}Tm_{20}Gd_{18}$ amorphous ribbons, J. Magn. Magn. Mater. 514 (2020) 167270, https://doi.org/10.1016/j.jmmm.2020.167270.
[41] C.M. Pang, C.C. Yuan, L. Chen, H. Xu, K. Guo, J.C. He, Y. Li, M.S. Wei, X.M. Wang, J.T. Huo, B.L. Shen, Effect of Yttrium addition on magnetocaloric properties of Gd-Co-Al-Ho high entropy metallic glasses, J. Non Cryst. Solids 549 (2020) 120354, https://doi.org/10.1016/j.jnoncrysol.2020.120354.
[42] Y.K. Zhang, B.B. Wu, D. Guo, J. Wang, Z.M. Ren, Magnetic properties and promising cryogenic magneto-caloric performances of $Gd_{20}Ho_{20}Tm_{20}Cu_{20}Ni_{20}$ amorphous ribbons, Chin. Phys. B 30 (2021) 017501, https://doi.org/10.1088/1674-1056/abc0d7.
[43] F.X. Qin, N.S. Bingham, H. Wang, H.X. Peng, J.F. Sun, V. Franco, S.C. Yu, H. Srikanth, M.H. Phan, Mechanical and magnetocaloric properties of Gd-based amorphous microwires fabricated by melt-extraction, Acta Mater. 61 (2013) 1284–1293, https://doi.org/10.1016/j.actamat.2012.11.006.
[44] H.X. Shen, D.W. Xing, J.L. Sánchez Llamazares, C.F. Sánchez-Valdés, H. Belliveau, H. Wang, F.X. Qin, Y.F. Liu, J.F. Sun, H. Srikanth, M.H. Phan, Enhanced refrigerant capacity in Gd-Al-Co microwires with a biphase nanocrystalline/amorphous structure, Appl. Phys. Lett. 108 (2016) 092403, https://doi.org/10.1063/1.4943137.
[45] H.F. Belliveau, Y.Y. Yu, Y. Luo, F.X. Qin, H. Wang, H.X. Shen, J.F. Sun, S.C. Yu, H. Srikanth, M.H. Phan, Improving mechanical and magnetocaloric responses of amorphous melt-extracted Gd-based microwires via nanocrystallization, J. Alloy. Compd. 692 (2017) 658–664, https://doi.org/10.1016/j.jallcom.2016.08.254.
[46] Y.F. Wang, F.X. Qin, Y.H. Wang, H. Wang, R. Das, M.H. Phan, H.X. Peng, Magnetocaloric effect of Gd-based microwires from binary to quaternary system, AIP Adv. 7 (2017) 056422, https://doi.org/10.1063/1.4975356.
[47] N.T.M. Duc, H.X. Shen, E.M. Clements, O. Thiabgoh, J.L. Sanchez Llamazares, C. F. Sanchez-Valdes, N.T. Huong, J.F. Sun, H. Srikanth, M.H. Phan, Enhanced refrigerant capacity and Curie temperature of amorphous $Gd_{60}Fe_{20}Al_{20}$ microwires, J. Alloy. Compd. 807 (2019) 151694, https://doi.org/10.1016/j.jallcom.2019.151694.
[48] N.T.M. Duc, H.X. Shen, E. Clements, O. Thiabgoh, J.L.S. Llamazares, C.F. Sanchez-Valdes, N.T. Huong, J.F. Sun, H. Srikanth, M.H. Phan, Critical magnetic and magnetocaloric behavior of amorphous melt-extracted $Gd_{50}(Co_{69.25}Fe_{4.25}Si_{13}B_{13.5})_{50}$ microwires, Intermetallics 110 (2019) 106479, https://doi.org/10.1016/j.intermet.2019.106479.
[49] N.T.M. Duc, H.X. Shen, O. Thiabgoh, N.T. Huong, J.F. Sun, M.H. Phan, Melt-extracted $Gd_{73.5}Si_{13}B_{13.5}/GdB_6$ ferromagnetic/antiferromagnetic microwires with excellent magnetocaloric properties, J. Alloy. Compd. 818 (2020) 153333, https://doi.org/10.1016/j.jallcom.2019.153333.
[50] H.X. Shen, L. Luo, Y. Bao, H.B.C. Yin, S.D. Jiang, L.Y. Zhang, Y.J. Huang, S.J. Feng, D.W. Xing, J.S. Liu, Z. Li, Y.F. Liu, J.F. Sun, M.H. Phan, New DyHoCo medium entropy amorphous microwires of large magnetic entropy change, J. Alloy. Compd. 837 (2020) 155431, https://doi.org/10.1016/j.jallcom.2020.155431.
[51] Y.F. Wang, Y.Y. Yu, H. Belliveau, N.T.M. Duc, H.X. Shen, J.F. Sun, J.S. Liu, F. X. Qin, S.C. Yu, H. Srikanth, M.H. Phan, Enhanced magnetocaloric performance in nanocrystalline/amorphous $Gd_3Ni/Gd_{65}Ni_{35}$ composite microwires, J. Sci. Adv. Mater. Dev. 6 (2021) 587–594, https://doi.org/10.1016/j.jsamd.2021.07.010.
[52] Y.F. Wang, N. Thi My Duc, T.F. Feng, H.J. Wei, F.X. Qin, M.H. Phan, Competing ferromagnetic and antiferromagnetic interactions drive the magnetocaloric tunability in $Gd_{55}Co_{30}Ni_xAl_{15-x}$ microwires, J. Alloy. Compd. 907 (2022) 164328, https://doi.org/10.1016/j.jallcom.2022.164328.
[53] L. Luo, J.Y. Law, H.X. Shen, L.M. Moreno-Ramírez, V. Franco, S. Guo, N.T.M. Duc, J.F. Sun, M.H. Phan, Enhanced magnetocaloric properties of annealed melt-extracted $Mn_{1.3}Fe_{0.6}P_{0.5}Si_{0.5}$ microwires, Metals 12 (2022) 1536, https://doi.org/10.3390/met12091536.
[54] L. Luo, H.X. Shen, L.Y. Zhang, Y.J. Huang, J.F. Sun, M.H. Phan, Giant magnetocaloric effect and hysteresis loss in $Mn_xFe_{2-x}P_{0.5}Si_{0.5}$ ($0.7 \leq x \leq 1.2$) microwires at ambient temperatures, J. Sci. Adv. Mater. Dev. 9 (2024) 100756, https://doi.org/10.1016/j.jsamd.2024.100756.
[55] L. Luo, H.X. Shen, L.Y. Zhang, J.F. Sun, M.H. Phan, Effect of Fe on the microstructure and magnetic transition of Mn-Fe-P-Si microwires, J. Alloy. Compd. 1003 (2024) 175579, https://doi.org/10.1016/j.jallcom.2024.175579.
[56] T.P.L. Nguyen, T.T. Bui, B.K. Doan, L.P. Bui, T.H. Luu, C.D. Tran, T.V.T. Tran, T. Yokozawa, H.T. Nguyen, Synthesis of a conjugated molecular triad based on 9,9-dioctyl-9H-fluorene for fluorescence sensing to determine mesotrione, Vietnam J. Sci. Technol. Eng. 65 (2023) 14, https://doi.org/10.31276/VJSTE.65(1).14-18.
[57] D. Turnbull, Under what conditions can a glass be formed? Contemp. Phys. 10 (1969) 473–488, https://doi.org/10.1080/00107516908204405.
[58] Z.P. Lu, Y. Li, S.C. Ng, Reduced glass transition temperature and glass forming ability of bulk glass forming alloys, J. Non Cryst. Solids 270 (2000) 103–114, https://doi.org/10.1016/S0022-3093(00)00064-8.
[59] Z.P. Lu, C.T. Liu, A new glass-forming ability criterion for bulk metallic glasses, Acta Mater. 50 (2002) 3501–3512, https://doi.org/10.1016/S1359-6454(02)00166-0.

[60] S. Schneider, P. Thiyagarajan, W.L. Johnson, Formation of nanocrystals based on decomposition in the amorphous $Zr_{41.2}Ti_{13.8}Cu_{12.5}Ni_{10}Be_{22.5}$ alloy, Appl. Phys. Lett. 68 (1996) 493–495, https://doi.org/10.1063/1.116377.
[61] L.Q. Xing, C. Bertrand, J.P. Dallas, M. Cornet, Nanocrystal evolution in bulk amorphous $Zr_{57}Cu_{20}Al_{10}Ni_8Ti_5$ alloy and its mechanical properties, Mater. Sci. Eng. A 241 (1998) 216–225, https://doi.org/10.1016/S0921-5093(97)00489-9.
[62] L. Deng, A. Gebert, L. Zhang, H.Y. Chen, D.D. Gu, U. Kühn, M. Zimmermann, K. Kosiba, S. Pauly, Mechanical performance and corrosion behaviour of Zr-based bulk metallic glass produced by selective laser melting, Mater. Des. 189 (2020) 108532, https://doi.org/10.1016/j.matdes.2020.108532.
[63] H. Fu, M. Zou, Q. Cao, V.K. Pecharsky, K.A. Gschneidner, L.S. Chumbley, Microstructure and magnetocaloric effects in partially amorphous $Gd_{55}Co_{15}Al_{30-x}Si_x$ alloys, Mater. Sci. Eng. A 528 (2011) 5219–5222, https://doi.org/10.1016/j.msea.2011.03.067.
[64] D.B. Duan, Y. Wu, H.T. Chen, X.Z. Wang, X.J. Liu, H. Wang, S.H. Jiang, Z.P. Lu, A strategy to design eutectic high-entropy alloys based on binary eutectics, J. Mater. Sci. Technol. 103 (2022) 152–156, https://doi.org/10.1016/j.jmst.2021.06.038.
[65] Z.J. Mo, J. Shen, L.Q. Yan, C.C. Tang, X.N. He, X.Q. Zheng, J.F. Wu, J.R. Sun, B. G. Shen, Magnetic properties and magnetocaloric effect in the $HoNi_{1-x}Cu_xIn$ (x=0, 0.1, 0.3, 0.4) intermetallic compounds, J. Magn. Magn. Mater. 354 (2014) 49–53, https://doi.org/10.1016/j.jmmm.2013.10.036.
[66] F. Yuan, J. Du, B.L. Shen, Controllable spin-glass behavior and large magnetocaloric effect in Gd-Ni-Al bulk metallic glasses, Appl. Phys. Lett. 101 (2012) 032405, https://doi.org/10.1063/1.4738778.
[67] J. Li, L. Xue, W.M. Yang, C.C. Yuan, J.T. Huo, B.L. Shen, Distinct spin glass behavior and excellent magnetocaloric effect in $Er_{20}Dy_{20}Co_{20}Al_{20}RE_{20}$ (RE = Gd, Tb and Tm) high-entropy bulk metallic glasses, Intermetallics 96 (2018) 90–93, https://doi.org/10.1016/j.intermet.2018.03.002.
[68] J. Du, Q. Zheng, E. Brück, K.H.J. Buschow, W.B. Cui, W.J. Feng, Z.D. Zhang, Spin-glass behavior and magnetocaloric effect in Tb-based bulk metallic glass, J. Magn. Magn. Mater. 321 (2009) 413–417, https://doi.org/10.1016/j.jmmm.2008.09.034.
[69] B. Banerjee, On a generalised approach to first and second order magnetic transitions, Phys. Lett. 12 (1964) 16–17, https://doi.org/10.1016/0031-9163(64)91158-8.
[70] C.M. Bonilla, J. Herrero-Albillos, F. Bartolomé, L.M. García, M. Parra-Borderías, V. Franco, Universal behavior for magnetic entropy change in magnetocaloric materials: an analysis on the nature of phase transitions, Phys. Rev. B 81 (2010) 224424, https://doi.org/10.1103/PhysRevB.81.224424.
[71] A. Chirkova, K.P. Skokov, L. Schultz, N.V. Baranov, O. Gutfleisch, T.G. Woodcock, Giant adiabatic temperature change in FeRh alloys evidenced by direct measurements under cyclic conditions, Acta Mater. 106 (2016) 15–21, https://doi.org/10.1016/j.actamat.2015.11.054.
[72] Q. Luo, J. Shen, Magnetocaloric-magnetoresistance correlation in a Gd-based amorphous ferromagnet, Intermetallics 92 (2018) 79–83, https://doi.org/10.1016/j.intermet.2017.09.019.
[73] M.E. Wood, W.H. Potter, General analysis of magnetic refrigeration and its optimization using a new concept: maximization of refrigerant capacity, Cryogenics 25 (1985) 667–683, https://doi.org/10.1016/0011-2275(85)90187-0.
[74] V. Franco, A. Conde, Scaling laws for the magnetocaloric effect in second order phase transitions: from physics to applications for the characterization of materials, Int. J. Refrig. 33 (2010) 465–473, https://doi.org/10.1016/j.ijrefrig.2009.12.019.
[75] V. Franco, J.S. Blázquez, A. Conde, Field dependence of the magnetocaloric effect in materials with a second order phase transition: a master curve for the magnetic entropy change, Appl. Phys. Lett. 89 (2006) 222512, https://doi.org/10.1063/1.2399361.
[76] J.Y. Law, V. Franco, L.M. Moreno-Ramírez, A. Conde, D.Y. Karpenkov, I. Radulov, K.P. Skokov, O. Gutfleisch, A quantitative criterion for determining the order of magnetic phase transitions using the magnetocaloric effect, Nat. Commun. 9 (2018) 2680, https://doi.org/10.1038/s41467-018-05111-w.
[77] H.B.C. Yin, J.Y. Law, Y.J. Huang, V. Franco, H.X. Shen, S.D. Jiang, Y. Bao, J.F. Sun, Design of Fe-containing GdTbCoAl high-entropy-metallic-glass composite microwires with tunable Curie temperatures and enhanced cooling efficiency, Mater. Des. 206 (2021) 109824, https://doi.org/10.1016/j.matdes.2021.109824.
[78] J.Y. Law, L.M. Moreno-Ramírez, Á. Díaz-García, A. Martín-Cid, S. Kobayashi, S. Kawaguchi, T. Nakamura, V. Franco, MnFeNiGeSi high-entropy alloy with large magnetocaloric effect, J. Alloy. Compd. 855 (2021) 157424, https://doi.org/10.1016/j.jallcom.2020.157424.
[79] V. Franco, J.S. Blázquez, A. Conde, The influence of Co addition on the magnetocaloric effect of Nanoperm-type amorphous alloys, J. Appl. Phys. 100 (2006) 064307, https://doi.org/10.1063/1.2337871.
[80] L. Xue, L.L. Shao, Z.D. Han, Q. Luo, H.B. Wang, J.T. Huo, Z.Z. Li, B.S. Zhang, J. B. Cheng, B.L. Shen, Tunable magnetocaloric effect in Gd-based metallic glasses microalloying elements with different magnetism, J. Non Cryst. Solids 576 (2022) 121222, https://doi.org/10.1016/j.jnoncrysol.2021.121222.
[81] L.M. Moreno-Ramírez, J.S. Blázquez, V. Franco, A. Conde, M. Marsilius, V. Budinsky, G. Herzer, Magnetocaloric response of amorphous and nanocrystalline Cr-containing Vitroperm-type alloys, J. Magn. Magn. Mater. 409 (2016) 56–61, https://doi.org/10.1016/j.jmmm.2016.02.087.
[82] H.B.C. Yin, J.Y. Law, Y.J. Huang, H.X. Shen, S.D. Jiang, S. Guo, V. Franco, J.F. Sun, Enhancing the magnetocaloric response of high-entropy metallic-glass by microstructural control, Sci. China Mater. 65 (2022) 1134–1142, https://doi.org/10.1007/s40843-021-1825-1.
[83] Z.P. Ma, P. Xu, J.Y. Ying, Y.K. Zhang, L.W. Li, Insight into the structural and magnetic properties of $RECo_{12}B_6$ (RE = Ce, Pr, Nd) compounds: a combined experimental and theoretical investigation, Acta Mater. 247 (2023) 118757, https://doi.org/10.1016/j.actamat.2023.118757.
[84] D.J. Thouless, Introduction to phase transitions and critical phenomena, Phys. Bull. 23 (1972) 224, https://doi.org/10.1088/0031-9112/23/4/018.
[85] V. Franco, J.S. Blázquez, B. Ingale, A. Conde, The magnetocaloric effect and magnetic refrigeration near room temperature: materials and models, Annu. Rev. Mater. Res. 42 (2012) 305–342, https://doi.org/10.1146/annurev-matsci-062910-100356.
[86] P. Lampen, M.H. Phan, H. Srikanth, K. Kovnir, P. Chai, M. Shatruk, Heisenberg-like ferromagnetism in 3d-4f $La_{0.75}Pr_{0.25}Co_2P_2$ with localized Co moments, Phys. Rev. B 90 (2014) 174404, https://doi.org/10.1103/PhysRevB.90.174404.
[87] M.H. Phan, G.T. Woods, A. Chaturvedi, S. Stefanoski, G.S. Nolas, H. Srikanth, Long-range ferromagnetism and giant magnetocaloric effect in type VIII $Eu_8Ga_{16}Ge_{30}$ clathrates, Appl. Phys. Lett. 93 (2008) 252505, https://doi.org/10.1063/1.3055833.
[88] A. Arrott, J.E. Noakes, Approximate equation of state for nickel near its critical temperature, Phys. Rev. Lett. 19 (1967) 786–789, https://doi.org/10.1103/PhysRevLett.19.786.
[89] M. Seeger, S.N. Kaul, H. Kronmüller, R. Reisser, Asymptotic critical behavior of Ni, Phys. Rev. B 51 (1995) 12585–12594, https://doi.org/10.1103/PhysRevB.51.12585.
[90] D. Kim, B. Revaz, B.L. Zink, F. Hellman, J.J. Rhyne, J.F. Mitchell, Tricritical point and the doping dependence of the order of the ferromagnetic phase transition of $La_{1-x}Ca_xMnO_3$, Phys. Rev. Lett. 89 (2002) 227202, https://doi.org/10.1103/PhysRevLett.89.227202.
[91] B. Widom, Equation of state in the neighborhood of the critical point, J. Chem. Phys. 43 (1965) 3898–3905, https://doi.org/10.1063/1.1696618.
[92] J.S. Kouvel, M.E. Fisher, Detailed magnetic behavior of nickel near its curie point, Phys. Rev. 136 (1964) A1626–A1632, https://doi.org/10.1103/PhysRev.136.A1626.
[93] L. Liang, X. Hui, C.M. Zhang, G.L. Chen, A Dy-based bulk metallic glass with high thermal stability and excellent magnetocaloric properties, J. Alloy. Compd. 463 (2008) 30–33, https://doi.org/10.1016/j.jallcom.2007.09.041.
[94] W. Sheng, J.Q. Wang, G. Wang, J.T. Huo, X.M. Wang, R.W. Li, Amorphous microwires of high entropy alloys with large magnetocaloric effect, Intermetallics 96 (2018) 79–83, https://doi.org/10.1016/j.intermet.2018.02.015.
[95] S.J. Wei, H.X. Shen, L.Y. Zhang, L. Luo, X.X. Tang, J.F. Sun, X.Q. Li, Microstructure and magnetocaloric properties of melt-extracted SmGdDyCoAl high-entropy amorphous microwires, Rare Met. 43 (2024) 1234–1242, https://doi.org/10.1007/s12598-023-02501-y.